Supplementary Information for:

Engineering of PMo_{12}@NiCo-LDH composite *via in-situ* encapsulation-reassembly strategy for highly selective photocatalytic reduction of CO_2 to CH_4

Huaiying Zhang, Dongyuan Cui, Tianyang Shen, Tong He, Danzhong Sun, Sai An*, Bo Qi, and Yu-Fei Song*

State Key Laboratory of Chemical Resource Engineering, Beijing University of Chemical Technology, Beijing 100029 P. R. China. *E-mail: songyf@mail.buct.edu.cn, ansai@mail.buct.edu.cn; Tel/Fax: +86 10-64431832.

List of contents

Figure S15. XPS spectra of Mo 3*d*, Ni 2*p* and Co 2*p* for as-prepared PMo_{12}@NiCo-LDH and recycled PMo_{12}@NiCo-LDH after CO_2PR.

Figure S16. Electrochemical impedance spectra (EIS), photocurrent-time profiles, room-temperature photoluminescence (PL) spectra of NiCo-LDH and PMo_{12}@NiCo-LDH.

Figure S17. UV-vis spectra and bandgaps calculated from Tauc plots of PMo_{12}@NiCo-LDH and NiCo-LDH; Mott-Schottky plots of PMo_{12}@NiCo-LDH and NiCo-LDH. valance band XPS spectra of PMo_{12}@NiCo-LDH and NiCo-LDH; conduction band minimum (CBM), valence band maximum (VBM) of PMo_{12}@NiCo-LDH and NiCo-LDH.

Figure S18. XPS spectra of O 1*s* for PMo_{12}@NiCo-LDH and recycled PMo_{12}@NiCo-LDH after the CO_2PR.

Table S1. Porosity properties of PMo_{12}@ZIF-67 and PMo_{12}@NiCo-LDH.

Table S2. Comparison of CO_2PR performance for various photocatalytic system in this work and in previous literature.

Experimental section

Chemicals and materials. Phosphomolybdic acid (PMo_{12}), methanol, ethanol, and acetonitrile were obtained from Fuchen (Tianjin) Chemical Reagent Co., Ltd. 2-methylimidazole (2-MIM), terpyridine ruthenium chloride ($Ru(bpy)_3Cl_2·6H_2O$, 98%), and triethanolamine (TEOA, 99%) were purchased from Energy chemical. Cobalt (II) nitrate hexahydrate ($Co(NO_3)_2·6H_2O$, 99%) and nickel (II) nitrate hexahydrate ($Co(NO_3)_2·6H_2O$, 99%) were purchased from Sigma-Aldrich trading Co., Ltd. High purity CO_2 (99.999%) and $^{13}CO_2$ (99%) were obtained from Linde Gas Co., Ltd. All the chemicals were used directly without any further purification.

Synthesis of PMo_{12}@ZIF-67. The synthesis of PMo_{12}@ZIF-67 referenced to the literature with tiny modification[1]. Typically, the mixture of 2.5 mmol $Co(NO_3)_2·6H_2O$ in 25 mL methanol and 10 mL aqueous solution contained certain amount of Keggin-type POMs $H_3PMo_{12}O_{40}$ (1.2×10^{-2} mmol, 25 mg) was stirred continuously at room temperature for 30 min. Subsequently, 40.0 mmol 2-methylimidazole in 25 mL methanol was dropwise added, and a purple suspension was produced. After stirring for 2.5 h, the bluish violet precipitate was collected *via* centrifugation, washing with methanol for several times, and drying at 60 °C in vacuum overnight. The obtained solid was denoted as PMo_{12}@ZIF-67. For comparison, ZIF-67 was prepared by the same method except for the absence of $H_3PMo_{12}O_{40}$.

Synthesis of PMo_{12}@NiCo-LDH. Firstly, $Ni(NO_3)_2·6H_2O$ (0.42 mmol, 120 mg) was dissolved in 25 mL ethanol with vigorous stirring for 30 min. Subsequently, 40 mg PMo_{12}@ZIF-67 was added into the above solution. After continuous stirring at room temperature for another 2 h, the precipitation was collected *via* centrifugation, washing with ethanol for several times, and drying at 60 °C in vacuum overnight. The resultant solid was denoted as PMo_{12}@NiCo-LDH.

Synthesis of NiCo-LDH. NiCo-LDH was prepared by the same method as PMo_{12}@NiCo-LDH, except for the replacement of PMo_{12}@ZIF-67 to ZIF-67.

Characterizations. High-resolution transmission electron microscopy (HRTEM) images were performed on a JEOL JEM-2200FS operating at 200 kV. Elemental mapping EDS spectra were recorded using energy dispersive spectroscopy attached to

JEOL JEM-2200FS. Scanning electron microscopy (SEM) images were performed on a Zeiss Supra55. Inductively coupled plasma atomic emission spectroscopy (ICP-AES) analysis was carried out on a Shimadzu ICPS-7500 instrument. Fourier transform infrared (FT-IR) spectra were collected on a Bruker Vector 22 infrared spectrometer using the KBr pellet method at wavenumbers ranging from 4000 to 400 cm^{-1}. X-ray diffraction (XRD) patterns were collected by a Rigaku XRD-6000 diffractometer equipped with a Cu Kα radiation (λ = 1.5405 Å). N_2 adsorption-desorption measurements were determined on a Micromeritics ASAP 2020 M surface area and porosity analyzer, with samples pre- degassing under vacuum at 100 °C for 6 h. X-ray photoelectron spectroscopy (XPS) spectra were performed on a monochromatized ALK exciting X-radiation (PHI Quantera SXM), which were calibrated against C 1*s* at 284.8 eV. Solid-state ultraviolet-visible (UV-vis) diffuse reflectance spectra were collected on a Beijing PGENERAL TU-1901 spectrometer, with wavelength ranging from 200 to 800 nm. *In-situ* diffuse reflectance infrared Fourier transform spectroscopy (*in-situ* DRIFT) was performed on a Bruker TENSOR II spectrometer.

CO_2 photocatalytic reduction (CO_2PR). The CO_2PR was carried out in a sealed stainless reactor (40 mL) with a quartz top window for light irradiation. In a typical run, 10 mg PMo_{12}@NiCo-LDH powder was dispersed in 10 mL solution with CH_3CN : H_2O : TEOA = 6 : 2 : 2 (v/v/v), following by addition of 4.4 $\times 10^{-3}$ mmol (3.3 mg) $Ru(bpy)_3Cl_2 \cdot 6H_2O$. The reactor was then sealed and evacuated by a vacuum pump to remove the residual air completely. High purity CO_2 was filled into the reactor, with the pressure of 0.18 MPa. Under the irradiation of visible light (400−800 nm) with continuous stirring for 1 h, the gaseous products were collected and analyzed qualitatively and quantitatively by Shimadzu GC-2014 gas chromatography equipped with both flame ionization detector (FID) and thermal conductivity detector (TCD). ^1H NMR spectra were collected on a Bruker AV400 NMR spectrometer at 400 MHz to detected the possible liquid products. The isotopic-labeled experiments were carried out with $^{13}CO_2$ instead of high purity $^{12}CO_2$ under the same condition. After irradiation for 1 h, the resultant products were collected and analyzed through gas chromatography-mass spectrometry (GC-MS, QP2020 equipped with Micropacked

column).

Electrochemical measurements. Electrochemical measurements were all performed on a CHI760A electrochemical workstation (Shanghai Chenhua, China) in a standard three-electrode quartz cell with 0.1 M Na_2SO_4 aqueous solution as the electrolyte. Electrochemical impedance spectroscopy (EIS) was recorded with carbon paper coated by PMo_{12}@NiCo-LDH or NiCo-LDH as a working electrode, Pt foil as a counter electrode, and Ag/AgCl (in saturated KCl) as a reference electrode. Transient photocurrent measurements and Mott-Schottky tests were measured with indium tin oxide (ITO) coated by PMo_{12}@NiCo-LDH or NiCo-LDH as a working electrode, Pt foil as a counter electrode, and Ag/AgCl (in saturated KCl) as a reference electrode.

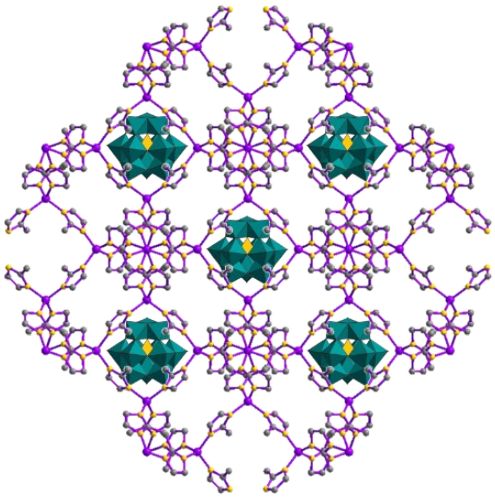

Figure S1. Topology diagram of the PMo_{12}@ZIF-67 precursor.

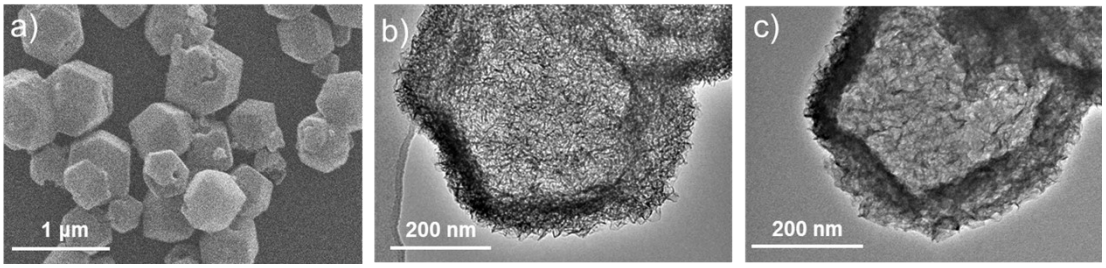

Figure S2. a) SEM images of PMo_{12}@ZIF-67; TEM images of **b)** as-prepared PMo_{12}@NiCo-LDH and **c)** recycled PMo_{12}@NiCo-LDH after CO_2PR.

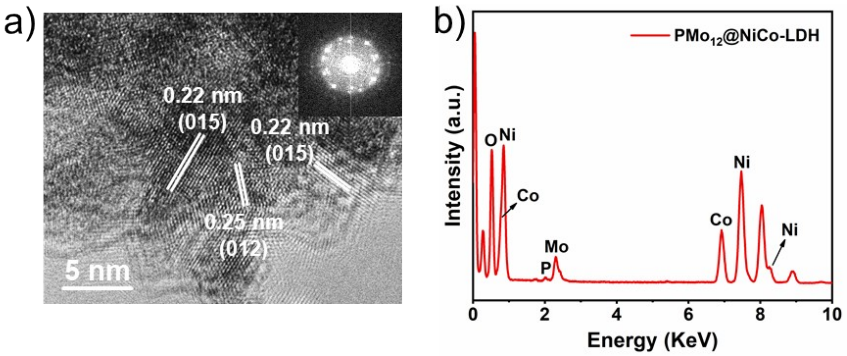

Figure S3. a) HRTEM image of PMo_{12}@NiCo-LDH with corresponding FFT diffraction pattern inside; **b)** EDS spectrum of PMo_{12}@NiCo-LDH.

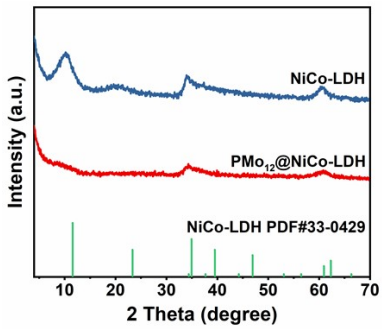

Figure S4. XRD patterns of PMo_{12}@NiCo-LDH and NiCo-LDH.

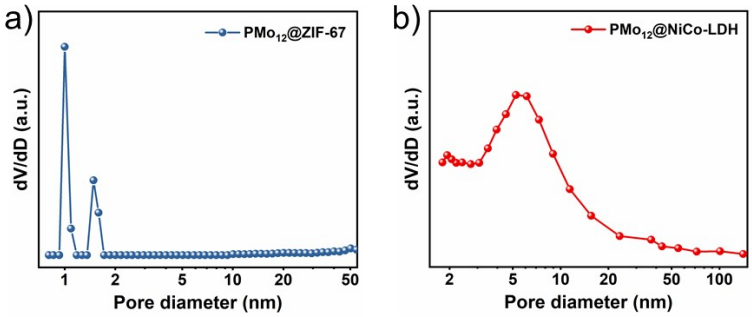

Figure S5. a) NLDFT pore size distribution profile of PMo_{12}@ZIF-67; **b)** BJH pore size distribution profile of PMo_{12}@NiCo-LDH.

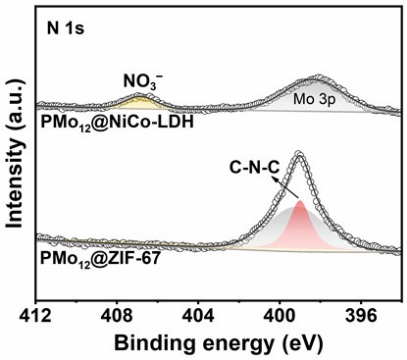

Figure S6. XPS spectra of N 1*s* for PMo_{12}@ZIF-67 and PMo_{12}@NiCo-LDH.

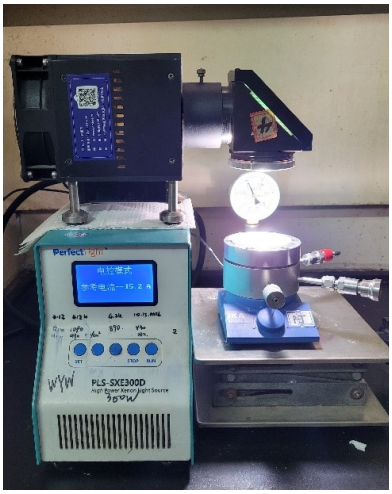

Figure S7. The figure of the experimental set up for CO_2PR.

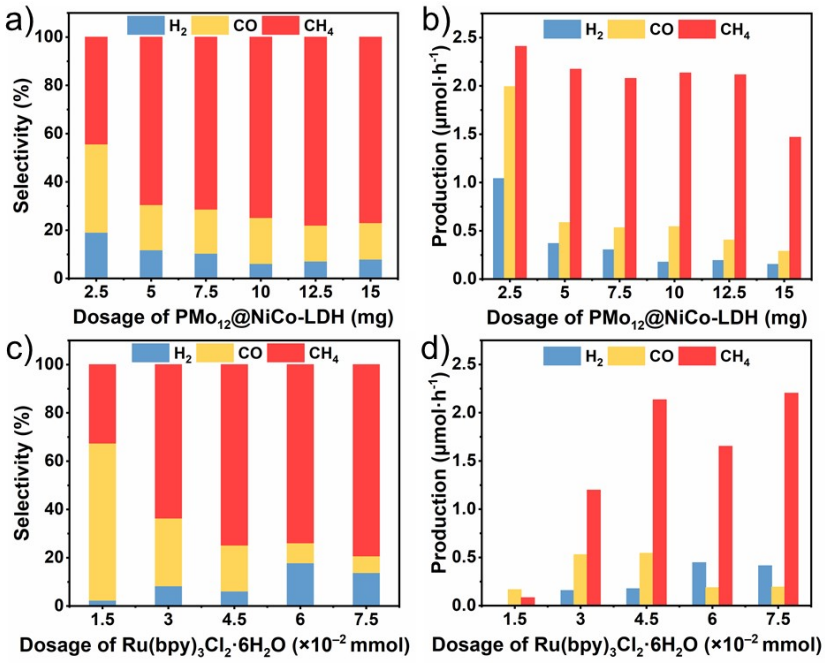

Figure S8. a) Selectivity and **b)** production rate of H_2, CO and CH_4 in CO_2PR with various dosage of PMo_{12}@NiCo-LDH; **c)** selectivity and **d)** production rate of H_2, CO and CH_4 for PMo_{12}@NiCo-LDH in CO_2PR with various dosage of $Ru(bpy)_3Cl_2 \cdot 6H_2O$.

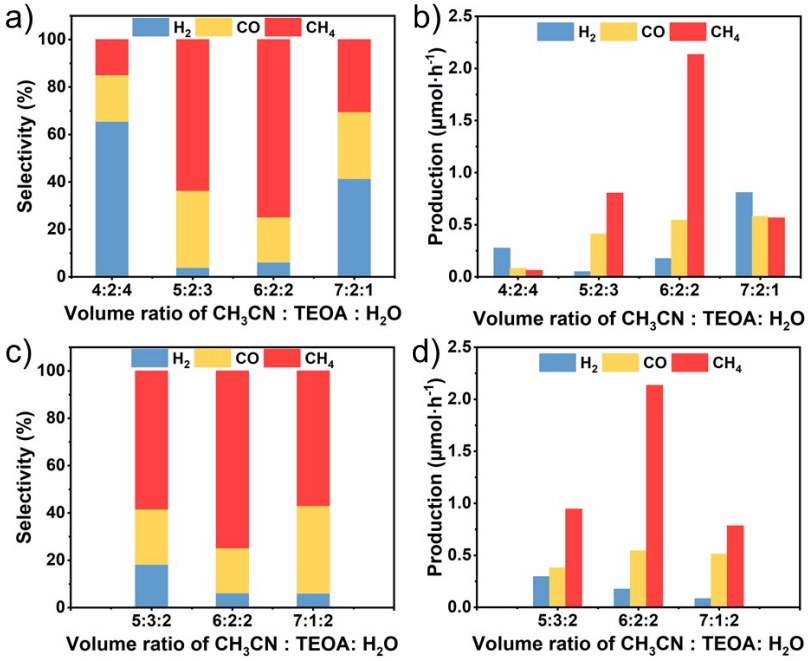

Figure S9. a), c) Selectivity and **b), d)** production rate of H_2, CO and CH_4 for PMo_{12}@NiCo-LDH in CO_2PR with various volume ratio of CH_3CN : TEOA : H_2O.

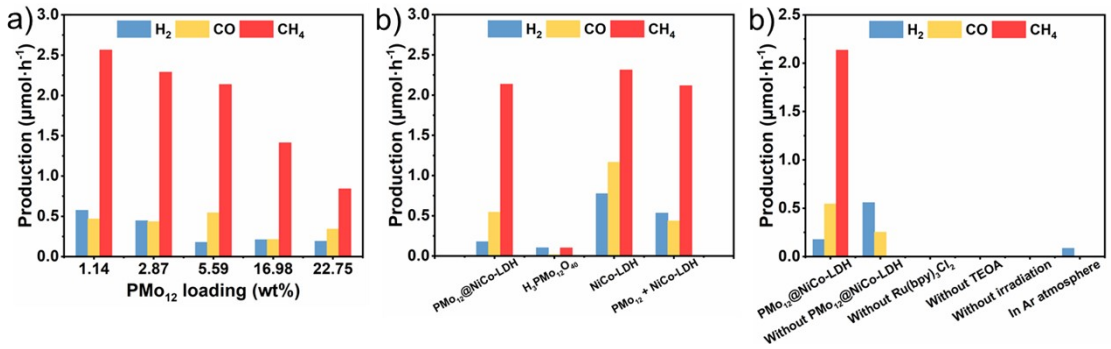

Figure S10. The influence of **a)** PMo_{12} loading, **b)** catalysts, **c)** reaction conditions on the production rate of H_2, CO and CH_4 in CO_2PR.

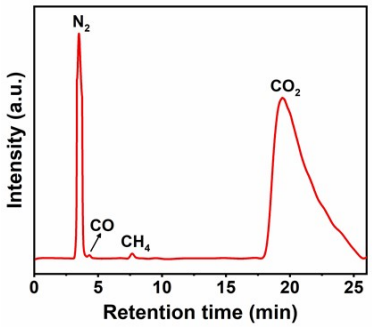

Figure S11. GC spectrum (connected to MS) of the reaction products for PMo_{12}@NiCo-LDH in CO_2PR.

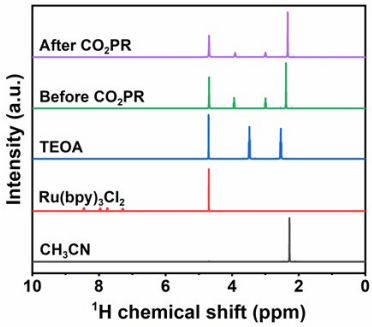

Figure S12. ^{1}H NMR spectra of CH_3CN, TEOA, $Ru(bpy)_3Cl_2 \cdot 6H_2O$ and the liquid mixture of reaction system before and after CO_2PR.

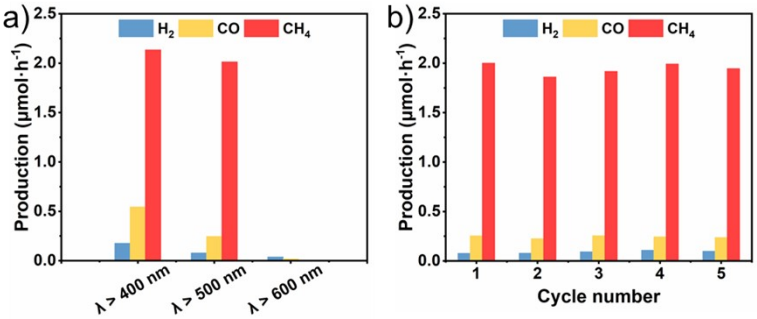

Figure S13. Production rate of H_2, CO and CH_4 in CO_2PR **a)** under irradiation of various wavelength and **b)** in various cycle numbers under $\lambda > 500$ nm.

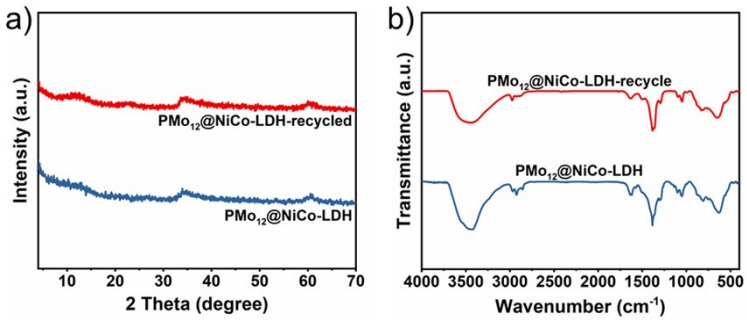

Figure S14. a) XRD patterns and **b)** FT-IR spectra of as-prepared PMo_{12}@NiCo-LDH and recycled PMo_{12}@NiCo-LDH after CO_2PR.

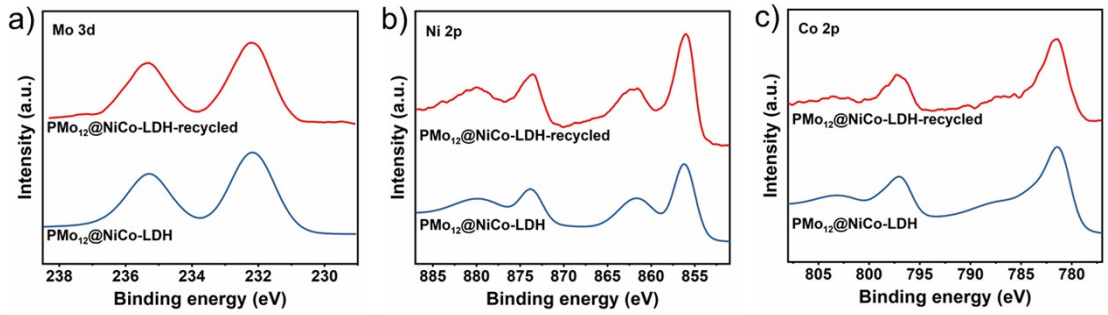

Figure S15. XPS spectra of **a)** Mo 3*d* **b)** Ni 2*p* and **c)** Co 2*p* for as-prepared PMo_{12}@NiCo-LDH and recycled PMo_{12}@NiCo-LDH after CO_2PR.

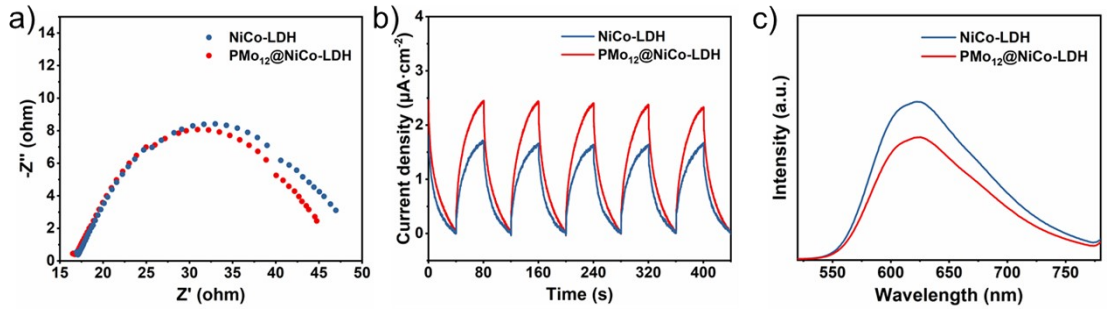

Figure S16. a) Electrochemical impedance spectra (EIS), **b)** photocurrent–time profiles, **c)** room-temperature photoluminescence (PL) spectra of NiCo-LDH and PMo_{12}@NiCo-LDH.

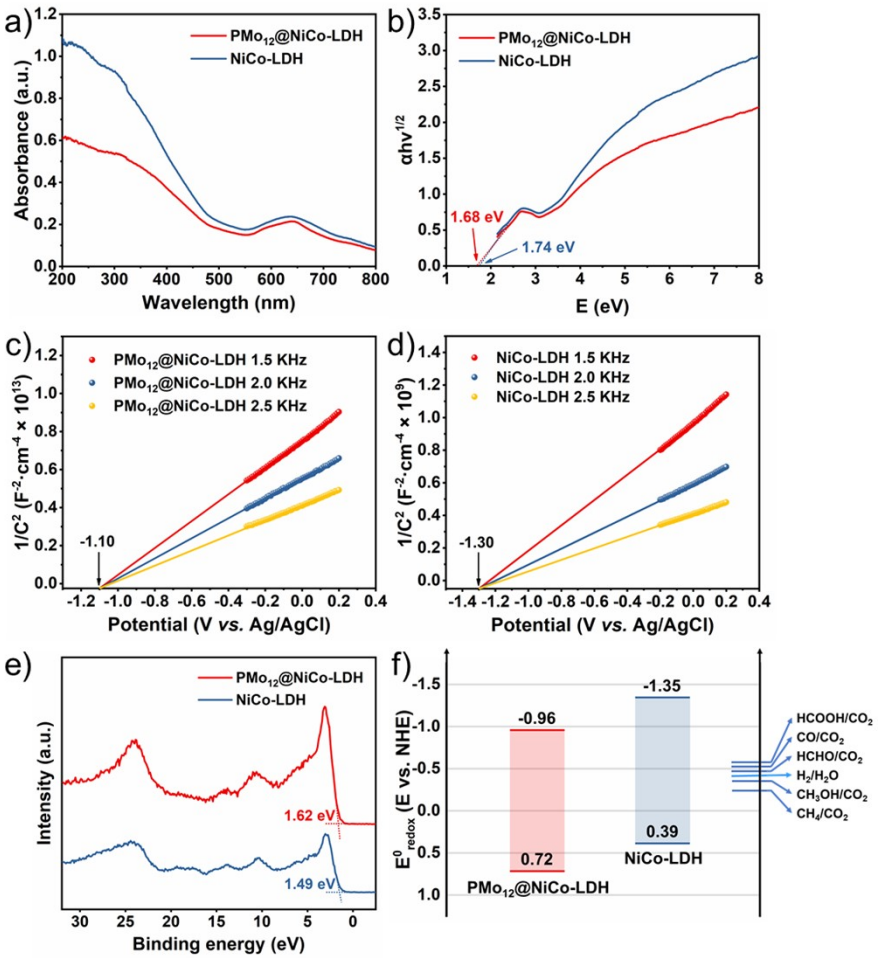

Figure S17. a) UV-vis spectra and **b)** bandgaps calculated from Tauc plots of PMo_{12}@NiCo-LDH and NiCo-LDH; Mott-Schottky plots of **c)** PMo_{12}@NiCo-LDH and **d)** NiCo-LDH. **e)** valance band XPS spectra of PMo_{12}@NiCo-LDH and NiCo-LDH; **f)** conduction band minimum (CBM), valence band maximum (VBM) of PMo_{12}@NiCo-LDH and NiCo-LDH.

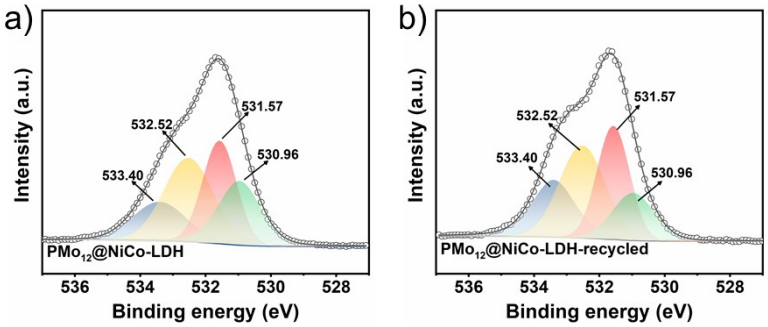

Figure S18. XPS spectra of O 1*s* for **a)** PMo_{12}@NiCo-LDH and **b)** recycled PMo_{12}@NiCo-LDH after the CO_2PR.

Table S1. Porosity properties of PMo_{12}@ZIF-67 and PMo_{12}@NiCo-LDH.

Catalyst	S_{BET} ($m^2 \cdot g^{-1}$)	V_{meso} ($cm^3 \cdot g^{-1}$)	V_{micro} ($cm^3 \cdot g^{-1}$)	D_p (nm)
PMo_{12}@ZIF-67	1187	0.15	0.55	1.0, 1.5
PMo_{12}@NiCo-LDH	190	0.54	–	6

Table S2. Comparison of CO_2PR performance for various photocatalytic system in this work and in previous literature.

Catalyst	Photosensitizer co-catalyst	Sacrificial agent	Solvent	Light source	Major product selectivity	Production rate ($\mu mol \cdot g^{-1} \cdot h^{-1}$)	Reference
NENU-606	$[Ru(bpy)_3]Cl_2 \cdot 6H_2O$	TEOA	H_2O	300 W Xe ($\lambda > 420$ nm)	CH_4: 85.5% CO: 14.5%	1.7478 0.2957	[2]
3D Fe–Mn POM structures	$[Ru(bpy)_3]Cl_2 \cdot 6H_2O$	TEOA	H_2O	280 W Xe ($\lambda = 415$ nm)	CH_4: 92.6% CO: 7.4%	1.440 0.115	[3]
TiO_2/NiAl-LDH	–	–	H_2O	300 W Xe Simulated-solar-light	CH_4: 81.8% CO: 9.9% H_2: 8.3%	20.56 2.48 2.08	[4]
$Cu_{2-x}S$/Ni-Al-LDH	–	–	H_2O	300 W Xe Simulated-solar-light	CH_4: 72.8% CO: 27.2 %	14.2 5.3	[5]

ZnCr-LDH/$Ti_3C_2T_x$	–	–	H_2O	300 W Xe (λ = 385 nm)	CH_4: 14% CO: 86%	19.95 μmol g^{-1} 122.45 μmol g^{-1}	[6]
Monolayer NiAl-LDH	$[Ru(bpy)_3]Cl_2·6H_2O$	TEOA	MeCN-H_2O (3 : 1 v/v)	300 W Xe (λ > 600 nm)	CH_4: 70.3% CO: 29.7%	103 43	[7]
HC-NiCo-LDH	$[Ru(bpy)_3]Cl_2·6H_2O$	TEOA	MeCN-H_2O (2 : 1 v/v)	300 W Xe (λ > 400 nm)	CH_4: 62.7% CO: 35.6 % H_2: 1.7%	560 311 29	[8]
Monolayer NiFe-LDH	$[Ru(bpy)_3]Cl_2·6H_2O$	TEOA	MeCN-H_2O (3 : 1 v/v)	300 W Xe (λ > 400 nm)	CH_4: 81.75% CO: 15.68% H_2: 2.57%	1.52 μmol·h^{-1} 0.29 μmol·h^{-1} 0.05 μmol·h^{-1}	[9]
PMo_{12}@NiCo-LDH	$[Ru(bpy)_3]Cl_2·6H_2O$	TEOA	MeCN-H_2O (3 : 1 v/v)	300 W Xe (λ > 400 nm)	CH_4: 74.8% CO: 19.0% H_2: 6.2%	2.13 μmol·h^{-1} 0.54 μmol·h^{-1} 0.18 μmol·h^{-1}	**This work**
PMo_{12}@NiCo-LDH	$[Ru(bpy)_3]Cl_2·6H_2O$	TEOA	MeCN-H_2O (3 : 1 v/v)	300 W Xe (λ > 500 nm)	CH_4: 86.2% CO: 10.5% H_2: 3.3%	2.01 μmol·h^{-1} 0.24 μmol·h^{-1} 0.08 μmol·h^{-1}	**This work**

Reference

[1] L. Zhang, T. Mi, M. A. Ziaee, L. Liang and R. Wang, Hollow POM@MOF hybrid-derived porous $Co_3O_4/CoMoO_4$ nanocages for enhanced electrocatalytic water oxidation, *J. Mater. Chem. A*, 2018, **6**, 1639-1647.

[2] S.-L. Xie, J. Liu, L.-Z. Dong, S.-L. Li, Y.-Q. Lan and Z.-M. Su, Hetero-metallic active sites coupled with strongly reductive polyoxometalate for selective photocatalytic CO_2-to-CH_4 conversion in water, *Chem. Sci.*, 2019, **10**, 185-190.

[3] Y. Benseghir, A. Solé-Daura, P. Mialane, J. m. Marrot, L. Dalecky, S. Béchu, M. Frégnaux, M. Gomez-Mingot, M. Fontecave, C. Mellot-Draznieks and A. Dolbecq, Understanding the photocatalytic reduction of CO_2 with heterometallic molybdenum(V) phosphate polyoxometalates in aqueous media, *ACS Catal.*, 2022, **23**, 453-464.

[4] W.-K. Jo, S. Moru and S. Tonda, A green approach to the fabrication of a TiO_2/NiAl-LDH core–shell hybrid photocatalyst for efficient and selective solar-powered reduction of CO_2 into value-added fuels, *J. Mater. Chem. A*, 2020, **8**, 8020-8032.

[5] X.-Y. Ji, R.-T. Guo, J.-Y. Tang, Y.-F. Miao, Z.-D. Lin, L.-F. Hong, Y. Yuan, Z.-S. Li and W.-G. Pan, Construction of full solar-spectrum-driven $Cu_{2-x}S$/Ni-Al-LDH heterostructures for efficient photocatalytic CO_2 reduction, *ACS Appl. Energy Mater.*, 2022, **5**, 2862-2872.

[6] B. Zhou, Y. Yang, Z. Liu, N. Wu, Y. Yan, Z. Wenhua, H. He, J. Du, Y. Zhang, Y. Zhou and Z. Zou, Boosting photocatalytic CO_2 reduction via Schottky junction with ZnCr layered double hydroxide nanoflakes aggregated on 2D $Ti_3C_2T_x$ cocatalyst, *Nanoscale*, 2022, **14**, 7538-7546.

[7] L. Tan, S.-M. Xu, Z. Wang, Y. Xu, X. Wang, X. Hao, S. Bai, C. Ning, Y. Wang, W. Zhang, Y. K. Jo, S.-J. Hwang, X. Cao, X. Zheng, H. Yan, Y. Zhao, H. Duan and Y.-F. Song, Highly selective photoreduction of CO_2 with suppressing H_2 evolution over monolayer layered double hydroxide under irradiation above 600 nm, *Angew. Chem. Int. Ed.*, 2019, **58**, 11860-11867.

[8] J. An, T. Shen, W. Chang, Y. Zhao, B. Qi and Y.-F. Song, Defect engineering of NiCo-layered double hydroxide hollow nanocages for highly selective photoreduction of CO_2 to CH_4 with suppressing H_2 evolution, *Inorg. Chem. Front.*, 2021, **8**, 996-1004.

[9] S. Bai, T. Li, H. Wang, L. Tan, Y. Zhao and Y.-F. Song, Scale-up synthesis of monolayer layered double hydroxide nanosheets via separate nucleation and aging steps method for efficient CO_2 photoreduction, *Chem. Eng. J.*, 2021, **419**, 129390.